Received: 18 May 2022 | Revised: 19 July 2022 | Accepted: 10 August 2022

DOI: 10.1002/htj.22679

ORIGINAL ARTICLE

HEAT TRANSFER WILEY

A numerical solution using EFDM for unsteady MHD radiative Casson nanofluid flow over a porous stretching sheet with stability analysis

Shiva Rao | **Paramananda Deka**

Department of Mathematics, Dibrugarh University, Dibrugarh, India

Correpsondence
Paramananda Deka, Department of Mathematics, Dibrugarh University, Dibrugarh, India.
Email: pndeka@dibru.ac.in

Abstract

The present study deals with the heat and mass transfer of the unsteady two-dimensional magneto-hydrodynamics Casson nanofluid flow over a non-linearly stretched porous sheet associated with viscous dissipation, chemical reaction, heat generation, and thermal radiation. After nondimensionalizing the boundary layer governing equations, an explicit finite difference scheme is implemented to solve the equations. To make the numerical approach more reliable, a stability analysis is carried out to establish the efficient convergence criteria ($Le \geq 0.25$ and $Pr \geq 0.373$). The velocity, temperature, and nanoparticle concentration profiles are plotted to investigate the influence of different flow parameters. It is found that the nanofluid motion hastens with the increase in both the Grashof number and the modified Grashof number. It is also noteworthy to observe that increasing thermal radiation enhances the nanofluid temperature, whereas increasing chemical reaction leads to a decrease in nanofluid concentration. The current research shows that there are some important industrial applications for magnetic nanoparticle processing and cooling in the industry. The study finds its importance with the view to increasing the heat and mass transfer efficiency

in industrial and engineering applications. The issues discussed in this study have not been included in the earlier investigation for unsteady Casson nanofluid flow due to a vertical stretching sheet of a porous medium. A comparative analysis of the results is also performed with previous studies to validate the efficiency of the numerical approach.

KEYWORDS

Casson nanofluid, chemical reaction, finite difference, MHD, porous, stretching sheet, thermal radiation, viscous dissipation

1 | INTRODUCTION

Consideration of nanofluids in industrial and engineering applications has drawn a lot of attention from scientists in the past few decades due to its improved thermal properties and advantageous heat transfer characteristics without the involvement of pressure drop phenomena. As a result of their high thermal conductivity, nanofluids are used in place of base fluids as working fluids these days. Nanofluids are made by the suspension of nanoparticles in the base fluid. Choi[1] was the first researcher to discover that the suspended nanoparticles in the base fluid could enhance thermal conductivity. Lee et al.[2] measured the thermal conductivity of different metal oxides and revealed that both shape and size played an important role in enhancing the thermal conductivity of the nanofluid. Nanoparticles not only increase thermal conductivity but also increase the heat transfer capacity by convection.[3] Eastman et al.[4] found that adding 1% of copper nanoparticles to ethylene glycol might boost thermal conductivity by 40%. Buonigiorno[5] sought to explain the rise in the thermal conductivity of the nanofluid by pointing out two main mechanisms for efficient augmentation of the thermal conductivity of the base fluid, namely Brownian motion and thermophoresis. Buongiorno's model[5] of viscous and incompressible nanofluid flow between a vertical flat plate and a porous medium was investigated by Nield and Kuznetsov.[6] Khan and Pop[7] investigated the evolution of heat transfer and nanoparticle volume fraction in a nanofluid across a stretching sheet. Makinde and Aziz[8] investigated the heat transfer properties of nanofluid flow utilizing convective boundary conditions. Rana and Bhargava[9] used the finite element method to solve Khan and Pop's problem for the nonlinearly stretching sheet. Khan et al.[10] studied the flow and heat transfer of water-based nanofluid with Fe_2O_3 as a nanoparticle across a porous medium with a low Darcy number. Recently, Hosseinzadeh et al.[11] studied the flow of magnetohydrodynamics (MHD) hybrid nanofluid (Fe_3O_4 and MoS_2) across a sinusoidal cylinder. Zangooee et al.[12] did a numerical study of how well heat moves through a three-dimensional MHD ferrofluid across a sheet that was stretching in both directions exponentially. Hosseinzadeh et al.[13] investigated the flow of non-Newtonian nanofluid of blood inside a porous vessel in the presence of a magnetic field.

Due to enormous practical applications, researchers are nowadays interested in surface-driven flows. Flow due to stretching/shrinking sheet has gained a lot of interest among researchers due to its application in several polymer industries as well as many manufacturing

processes. Akbar et al.[14] used the Buongiorno model to study the MHD double diffusive nanofluid over a linearly stretching sheet. Reddy et al.[15] analyzed and compared different non-Newtonian nanofluids across a stretching sheet, considering the effect of Joule heating and thermophoresis. An investigation into mixture-based dusty hybrid nanofluid flow taking ethylene glycol as a base fluid due to a porous stretching sheet was done by Rostami et al.[16] Ahmad et al.[17] used the lie group analysis technique to investigate the effect of thermal radiation and magnetic field on the hyperbolic tangent fluid across a stretching sheet.

As a result of a large number of applications it has in the engineering and technological fields, thermal radiation on free convection flow has become an extremely important topic in recent years. In particular, it has been proven useful in the design of space technology, components and equipment, and gas turbines. Unlike conduction and convection, thermal radiation does not need any medium to transmit heat. These properties make thermal radiation highly significant in the heat transfer of MHD nanofluid as it reduces the loss of heat. According to England and Emery,[18] for both absorbing and nonabsorbing gases, thermal radiation affected the flow of a natural convective boundary layer across a vertical plate. Shakhaoath et al.[19] used the finite difference method to study the thermal radiation effect of the unsteady MHD nanofluid flow passing over a stretched sheet. A nanofluid model was presented by Kumar et al.[20] with the purpose of describing flow and heat transmission across an infinite vertical plate in the presence of a magnetic field with viscous dissipation. In a subsequent study, Ali et al.[21] investigated the effect on the flow of MHD hybrid nanofluid of the thermal radiation and the nonuniform heat flux across the stretching cylinder. Ahmed et al.[22] investigated the issue of thermal radiation and heat flux affecting MHD laminar fluid flow when a sheet stretches. Lv et al.[23] used a numerical method to study the effect of hall currents on the flow of nanofluids in a rotating channel. Rama Devi and Reddy[24] investigated the effect of entropy generation along with thermal radiation and chemical reaction on hybrid nanofluid due to stretching of the sheet.

Non-Newtonian fluids, such as dissolved polymers, glues, paints, asphalts, and biological solutions, have been extensively employed in many industrial and technological areas. Non-Newtonian fluids do not comply with Newton's law of viscosity, that is, shear stress is not directly proportional to the gradient of velocity. In 1959, Casson developed the viscoelastic fluid model known as Casson fluid. The Casson fluid demonstrates zero viscosity at infinite shear rates and infinite viscosity at zero shear rates, resulting in stress under which no flow is possible. Tomato sauce, honey, soup, human blood, and orange juice are all examples of Casson fluid. Using the homotopy analysis method for solving differential equations, Ibrahim et al.[25] investigated the influence of a chemical reaction and a heat source on the dissipative MHD flow of Casson nanofluid over a stretched sheet. They have looked into the effect of the Casson parameter and the suction parameter on the rate at which heat and mass are transferred. Reddy et al.[26] investigated the flow of a three-dimensional MHD Casson nanofluid caused by a stretching sheet and the effects of thermal radiation, a heat source/sink, and double stratification. The radiation impact on Casson nanofluid was studied by Shashikumar et al.,[27] who conducted their research on the flow between vertical plates. Rafique et al.[28] used a nonlinear inclined surface to numerically study the impact of Soret and Dufour effects on the nanofluid flow. Lund et al.[29] performed a stability analysis on MHD Casson nanofluid through an exponentially stretching and shrinking sheet. Reza-E-Rabbi[30] used a finite difference method to study an unsteady MHD Casson nanofluid, taking into account the effects of Brownian motion and the thermophoresis parameter. Abdal et al.[31] examined the Casson

nanofluid flow under a magnetic field over an extending cylinder. Recently, much progress has been made in the study of how the Casson fluid moves in a peristaltic motion.

In the unsteady MHD Casson nanofluid flow across a vertical porous stretching sheet investigation on the impact of thermal radiation, chemical reaction, a heat source, and viscous dissipation remained unexplored so far, we have noticed. We are motivated to carry out the present study to cover some of the interesting issues pertaining to the effect of thermal radiation and associate factors on the unsteady flow of Casson nanofluid in a porous stretching sheet. This numerical investigation covers the following aspects:

- To consider a suitable mathematical model involving governing equations and boundary conditions for the Casson nanofluid MHD flow across the vertical porous stretching sheet
- Nondimensionalization of the governing equations and implementation of the explicit finite difference method.
- Plotting graph for the velocity, temperature, and nanoparticle concentration distribution for different physical parameters.
- To compare the obtained results with previous work to validate the efficiency of the numerical approach.
- To analyze the stability and convergence of the computed values of flow variables.

2 | MATHEMATICAL MODEL OF THE FLOW

A two-dimensional unsteady higher-order chemically reactive MHD Casson nanofluid flow from a permeable stretching sheet is examined under the influence of heat generation, thermal radiation, and viscous dissipation. The x-axis is taken tangential and it is in the vertical direction along the sheet, whereas the y-axis is normal to the sheet in the Cartesian coordinate system. The physical model with the coordinate system of the flow is shown in Figure 1.

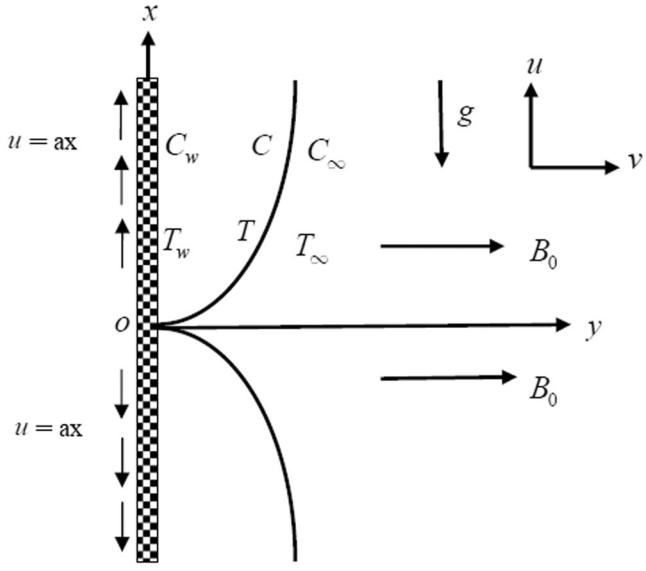

FIGURE 1 Schematic diagram of the problem

On the x-axis, two equal and opposing forces are applied to stretch the sheet while simultaneously maintaining the origin. At the beginning (at time $t = 0$), the fluid and the sheet are both in a state of stillness. However, later on, the sheet is stretched with a constant velocity, U_o in its own plane, which causes the fluid to start moving. The direction of flow is shown by $y > 0$. At time $t > 0$, the temperature and the nanoparticle concentration both increased to $T_w(>T_\infty)$ and, $C_w(>C_\infty)$, respectively, and remained constant after that. In this scenario, T_w, C_w are the temperature and nanoparticle concentration at the wall, and, T_∞, C_∞ are the temperature and nanoparticle concentration far away from the wall, respectively. In the y-direction, a uniform magnetic field strength B_o is applied. Under the above assumptions, the governing equations of the nanofluid can be written in vector form using Cartesian coordinates x and y as

The continuity equation:

$$\vec{\nabla} \cdot \vec{q} = 0. \tag{1}$$

The momentum equation:

$$\rho\left[\frac{\partial \vec{q}}{\partial t} + (\vec{q} \cdot \vec{\nabla})\vec{q}\right] = -\vec{\nabla} p + \mu\nabla^2\vec{q} - \vec{J} \times \vec{B} + \vec{g}\,\beta_t(T - T_\infty) + \vec{g}\,\beta_c(C - C_\infty) - \left(\frac{\mu}{k_0}\right)\vec{q}. \tag{2}$$

Ohm's law:

$$\vec{J} = \sigma[\vec{E} + (\vec{q} \times \vec{B})]. \tag{3}$$

Gauss law of magnetism:

$$\vec{\nabla} \cdot \vec{B} = 0. \tag{4}$$

The energy equation:

$$\begin{aligned}\rho C_p\left[\frac{\partial T}{\partial t} + (\vec{q} \cdot \vec{\nabla})T\right] = \kappa\nabla^2 T + \mu \quad (\nabla\vec{q} \cdot \nabla\vec{q}) - \nabla q_r + Q_0(T - T_\infty) \\ + \rho C_p\left[D_B(\vec{\nabla} C \cdot \vec{\nabla} T) + \left(\frac{D_T}{T_\infty}\right)(\vec{\nabla} T \cdot \vec{\nabla} T)\right].\end{aligned} \tag{5}$$

The concentration equation:

$$\frac{\partial C}{\partial t} + (\vec{q} \cdot \vec{\nabla})C = D_B\nabla^2 C + \frac{D_T}{T_\infty}\nabla^2 T - K_1(C - C_\infty). \tag{6}$$

Here we consider $\vec{q}$ is a function of u and v.

The rheological equations of Casson fluid for an incompressible and isotropic flow are given by[32,33]:

$$\tau_{ij} = \begin{cases} \left(\mu_B + \dfrac{p_y}{\sqrt{2\pi}}\right)2e_{ij}, & \pi < \pi_c \\ \left(\mu_B + \dfrac{p_y}{\sqrt{2\pi_c}}\right)2e_{ij}, & \pi < \pi_c \end{cases} \tag{7}$$

where e_{ij} is the rate of the strain tensor, μ_B is the Casson coefficient of viscosity, $p_y = \frac{\mu_b\sqrt{2\pi}}{\beta}$ is the yield stress of the fluid, $\pi = e_{ij}e_{ij}$, and π_c is the critical value of the product in these Casson model. Hence $\upsilon' = \upsilon\left(1 + \frac{1}{\beta}\right)$.

Based on a scale analysis, we put forward a standard boundary layer approximation on the unsteady MHD Casson nanofluid flow with heat and mass transfer and is governed by the following equations with the aforesaid assumptions and relevant boundary conditions[6,24–35]:

The continuity equation:

$$\frac{\partial u}{\partial x} + \frac{\partial v}{\partial y} = 0. \tag{8}$$

The momentum equation:

$$\begin{aligned} \frac{\partial u}{\partial t} + u\frac{\partial u}{\partial x} + v\frac{\partial v}{\partial y} = U_o\frac{\partial U_o}{\partial x} + \upsilon\left(1 + \frac{1}{\beta}\right)\frac{\partial^2 u}{\partial y^2} - \frac{\sigma_e B_o^2}{\rho}(u - U_o) + g\beta_t(T - T_\infty) \\ + g\beta_c(C - C_\infty) - \frac{u\upsilon}{k_o}\left(1 + \frac{1}{\beta}\right). \end{aligned} \tag{9}$$

The energy equation:

$$\begin{aligned} \frac{\partial T}{\partial t} + u\frac{\partial T}{\partial x} + v\frac{\partial T}{\partial y} = \alpha\frac{\partial^2 T}{\partial y^2} + \frac{\upsilon}{C_p}\left(1 + \frac{1}{\beta}\right)\left(\frac{\partial u}{\partial y}\right)^2 + \tau^*\left\{D_B\left(\frac{\partial C}{\partial y}\frac{\partial T}{\partial y}\right) + \frac{D_T}{T_\infty}\left(\frac{\partial T}{\partial y}\right)^2\right\} \\ - \frac{1}{\rho C_p}\frac{\partial q_r}{\partial y} + \frac{Q_o}{\rho C_p}(T - T_\infty). \end{aligned} \tag{10}$$

The concentration equation:

$$\frac{\partial C}{\partial t} + u\frac{\partial C}{\partial x} + v\frac{\partial C}{\partial y} = D_B\frac{\partial^2 C}{\partial y^2} + \frac{D_T}{T_\infty}\frac{\partial^2 T}{\partial y^2} - K_1(C - C_\infty). \tag{11}$$

The initial and boundary conditions are as follows:

$$\begin{array}{llllll} t=0, & u_w=U_o=ax, & v=0, & T=T_\infty, & C=C_\infty & \text{everywhere} \\ t\geq 0, & u=0, & v=0, & T=T_\infty, & C=C_\infty & \text{at } x=0 \\ & u=U_o=ax, & v=0, & T=T_w, & C=C_w & \text{at } y=0 \\ & u=0, & v=0, & T\to T_\infty, & C\to C_\infty & \text{at } y\to\infty \end{array} \tag{12}$$

Here q_r is the radiative heat flux term which by Rosseland approximation can be expressed as[36–38]:

$$q_r=\frac{-4\sigma^*}{3k^*}\frac{\partial T^4}{\partial y}, \tag{13}$$

where σ^* and k^* are Stefan-Boltzmann and mean absorption coefficients, respectively.

Expanding the Taylor series and neglecting the higher order, we get

$$T^4=4T_\infty^3T-3T_\infty^4.$$

Hence Equation (13) becomes

$$\frac{\partial q_r}{\partial y}=-\frac{16\sigma' T_\infty^3}{3k^*}\frac{\partial^2 T}{\partial y^2}. \tag{14}$$

Introducing the dimensionless variable[39]:

$$U=\frac{u}{U_o},V=\frac{v}{U_o},X=\frac{xU_o}{\upsilon},Y=\frac{yU_o}{\upsilon},\tau=\frac{tU_0^2}{\nu},\overline{T}=\frac{T-T_\infty}{T_w-T_\infty},\overline{C}=\frac{C-C_\infty}{C_w-C_\infty}. \tag{15}$$

Then Equations (8)–(11) become:

$$\frac{\partial U}{\partial X}+\frac{\partial V}{\partial Y}=0, \tag{16}$$

$$\frac{\partial U}{\partial \tau}+U\frac{\partial U}{\partial X}+V\frac{\partial U}{\partial Y}=\left(1+\frac{1}{\beta}\right)\frac{\partial^2 U}{\partial Y^2}+M(1-U)+\frac{1}{Re}\left(\frac{b^2}{a^2}\right)+G_r\overline{T}+G_m\overline{C}-K_pU\left(1+\frac{1}{\beta}\right), \tag{17}$$

$$\frac{\partial \overline{T}}{\partial \tau}+U\frac{\partial \overline{T}}{\partial X}+V\frac{\partial \overline{T}}{\partial Y}=\frac{1}{Pr}(1+R)\frac{\partial^2 \overline{T}}{\partial Y^2}+Nb\frac{\partial \overline{C}}{\partial Y}\frac{\partial \overline{T}}{\partial Y}+Nt\left(\frac{\partial \overline{T}}{\partial Y}\right)^2+Ec\left(1+\frac{1}{\beta}\right)\left(\frac{\partial U}{\partial Y}\right)^2+Q\overline{T}, \tag{18}$$

$$\frac{\partial \overline{C}}{\partial \tau}+U\frac{\partial \overline{C}}{\partial X}+V\frac{\partial \overline{C}}{\partial Y}=\frac{1}{Le}\left[\frac{\partial^2 \overline{C}}{\partial Y^2}+\frac{Nt}{Nb}\frac{\partial^2 \overline{T}}{\partial Y^2}\right]-\gamma\overline{C}. \tag{19}$$

The nondimensional boundary conditions are:

$$\begin{aligned} &\tau \le 0,\ U=0,\ V=0,\ \overline{T}=0\ \ \overline{C}=0 \ \text{everywhere}\\ &\tau > 0,\ U=0,\ V=0,\ \overline{T}=0\ \ \overline{C}=0 \ \text{at}\ \ X=0\\ &\qquad U=1,\ V=0,\ \overline{T}=1,\ \ \overline{C}=1 \ \text{at}\ \ Y=0\\ &\qquad U=0,\ V=0,\ \overline{T}=0,\ \ \overline{C}=0 \ \text{as}\ \ Y\to\infty \end{aligned} \tag{20}$$

The flow parameters involved in this investigation are defined in the following way-

$$Re=\frac{xu_w}{\upsilon},\quad M=\frac{\sigma_e B_o^2\upsilon}{\rho U_o^2},\quad G_r=\frac{g\beta_t(T_w-T_\infty)\upsilon}{U_o^3},\quad G_m=\frac{g\beta_c(C_w-C_\infty)\upsilon}{U_o^3},\quad K_p=\frac{\upsilon^2}{k_o U_o^2},$$
$$R=\frac{16\sigma^* T_\infty^3}{3\kappa\kappa^*},\quad Pr=\frac{\upsilon\rho C_p}{\kappa},\quad Ec=\frac{U_o^2}{C_p(T_w-T_\infty)},\quad N_b=\frac{\tau^* D_B(C_w-C_\infty)}{\upsilon},\quad Nt=\frac{\tau^* D_T(T_w-T_\infty)}{T_\infty\upsilon},$$
$$Le=\frac{\upsilon}{D_B},\quad Q=\frac{Q_o\upsilon}{\rho C_p U_o^2},\quad \gamma=\frac{\upsilon K_1(C_w-C_\infty)}{U_o^2}.$$

3 | NUMERICAL PROCEDURE

For solving the nonlinear coupled partial differential Equations (16)–(17) with boundary conditions (20) an explicit finite differential system of equations is implemented.

Here we consider a finite difference space grid where the x-axis is considered parallel to the sheet and the y-axis is normal to the sheet. We assume the sheet height to be $X_{\max}=100$, that is, X ranges from 0 to 100, and $Y_{\max}=25$ is supposed to correspond to Y, that is, Y ranges from 0 to 25. As illustrated in Figure 2, there is a space griding number of $m=125$ and $n=125$ along the X- and Y-axes, respectively.

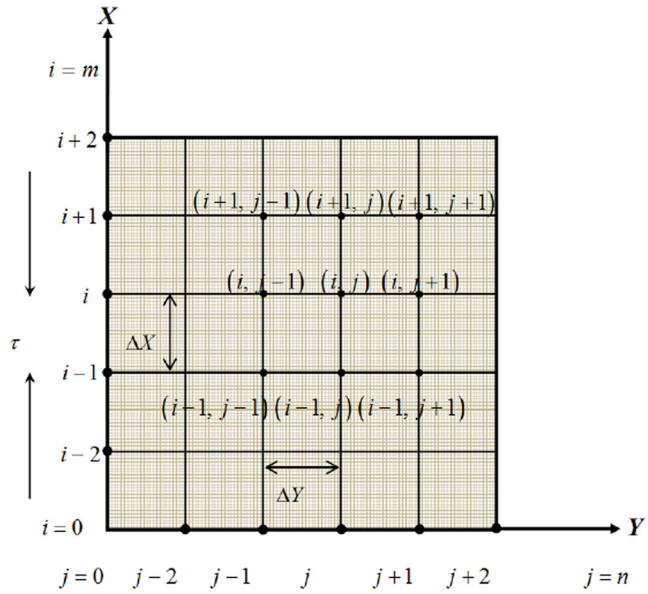

FIGURE 2 Finite difference space grid

U', V', $\overline{T}'$, and $\overline{C}'$ can be taken to be the values of U, V, $\bar{T}$, and $\overline{C}$, respectively at the end of a time-step. The following sets of finite difference equations are obtained via an explicit finite difference scheme:

$$\frac{U_{i,j} - U_{i-1,j}}{\Delta X} + \frac{V_{i,j} - V_{i,j-1}}{\Delta Y} = 0, \tag{21}$$

$$\frac{U'_{i,j} - U_{i,j}}{\Delta \tau} + U_{i,j}\frac{U_{i,j} - U_{i-1,j}}{\Delta X} + V_{i,j}\frac{U_{i,j+1} - U_{i,j}}{\Delta Y} = \frac{1}{Re}\left(\frac{b^2}{a^2}\right) + \left(1 + \frac{1}{\beta}\right)\frac{U_{i,j+1} - 2U_{i,j} + U_{i,j-1}}{(\Delta Y)^2} + M(1 - U_{i,j}) + G_r\bar{T}_{i,j} + G_m\bar{C}_{i,j} - K_pU_{i,j}\left(1 + \frac{1}{\beta}\right), \tag{22}$$

$$\frac{\overline{T}'_{i,j} - \overline{T}_{i,j}}{\Delta \tau} + U_{i,j}\frac{\overline{T}_{i,j} - \overline{T}_{i,j-1}}{\Delta X} + V_{i,j}\frac{\overline{T}_{i,j+1} - \overline{T}_{i,j}}{\Delta Y} = \left(\frac{1 + R}{Pr}\right)\frac{\overline{T}_{i,j+1} - 2\overline{T}_{i,j} + \overline{T}_{i,j-1}}{(\Delta Y)^2} + E_c\left(1 + \frac{1}{\beta}\right)\left(\frac{U_{i,j+1} - U_{i,j}}{\Delta Y}\right)^2 + Nb\left(\frac{\overline{T}_{i,j+1} - \overline{T}_{i,j}}{\Delta Y}\quad\frac{\overline{C}_{i,j+1} - \overline{C}_{i,j}}{\Delta Y}\right) + Nt\left(\frac{\overline{T}_{i,j+1} - \overline{T}_{i,j}}{\Delta Y}\right)^2 + Q\overline{T}_{i,j}, \tag{23}$$

$$\frac{\overline{C}'_{i,j} - \overline{C}_{i,j}}{\Delta \tau} + U_{i,j}\frac{\overline{C}_{i,j} - \overline{C}_{i-1,j}}{\Delta X} + V_{i,j}\frac{\overline{C}_{i,j+1} - \overline{C}_{i,j}}{\Delta Y} = \frac{1}{Le}\left[\frac{\overline{C}_{i,j+1} - 2\overline{C}_{i,j} + \overline{C}_{i,j-1}}{(\Delta Y)^2} + \frac{Nt}{Nb}\left(\frac{\overline{T}_{i,j+1} - 2\overline{T}_{i,j} + \overline{T}_{i,j-1}}{(\Delta Y)^2}\right)\right] - \gamma\overline{C}_{i,j}, \tag{24}$$

with initial and boundary conditions:

$$\begin{array}{lll} \text{When, } t \le 0 & \text{then} & U_{0,j} = 0,\quad V_{0,j} = 0,\quad \overline{T}_{0,j} = 0,\quad \overline{C}_{0,j} = 0 \quad \text{everywhere} \\ \text{When, } t > 0 & \text{then} & U_{0,j} = 1,\quad V_{0,j} = 0,\quad \overline{T}_{0,j} = 1,\quad \overline{C}_{0,j} = 1 \quad \text{for all} \quad R = 1 \\ & & U_{n,j} = 0,\quad V_{n,j} = 0,\quad \overline{T}_{n,j} = 0,\quad \overline{C}_{n,j} = 0 \quad 0 \quad \text{as} \quad R \to \infty \end{array} \tag{25}$$

where i and j represent the grid points with X and Y coordinates, respectively and the superscript n represents the value of time, $\tau = n.\ \Delta\tau$, where $n = 1,2,3,4,\ldots$ Along the x and y directions, each mesh size is held constant at $X = 0.8$ and $Y = 0.2$, with a lower time step of $\tau = 0.005$.

4 | STABILITY AND CONVERGENCE ANALYSIS

As the finite difference scheme implemented in the problem is explicit, it is very important to discuss the stability and convergence analysis. Equation (21) is overpassed as $\Delta\tau$ does not appear in it. For an arbitrary time $\tau = 0$, the Fourier expansion of U, T, and C are generally

expressed as $e^{i\alpha X}e^{i\beta Y}$ apart from the constants. Here $i = \sqrt{-1}$. At time t, the following equations can be obtained:

$$U : \psi(\tau)e^{i\alpha X}e^{i\beta Y},$$

$$\overline{T} : \theta(\tau)e^{i\alpha X}e^{i\beta Y}, \tag{26}$$

$$\overline{C} : \phi(\tau)e^{i\alpha X}e^{i\beta Y},$$

$$U' : \psi'(\tau)e^{i\alpha X}e^{i\beta Y},$$

$$\overline{T}' : \theta'(\tau)e^{i\alpha X}e^{i\beta Y}, \tag{27}$$

$$\overline{C}' : \boldsymbol{\phi}'(\tau)e^{i\alpha X}e^{i\beta Y}.$$

Substituting Equations (26) and (27) into Equations (22)–(24) we get:

$$\begin{aligned}\frac{\psi'(\tau)-\psi(\tau)}{\Delta\tau} + U\psi(\tau)\frac{(1-e^{-i\alpha\Delta X})}{\Delta X} + V\psi(\tau)\frac{(e^{i\beta\Delta Y}-1)}{\Delta Y}\\ = \left\{\frac{1}{Re}\left(\frac{b^2}{a^2}\right) + M(1-U)\right\}e^{-i\alpha X}e^{-i\beta Y} + 2\psi(\tau)\left(1+\frac{1}{\beta}\right)\frac{(cos\beta\Delta Y)-1)}{(\Delta Y)^2}\\ + G_r\theta(\tau) + G_m\phi(\tau) - \left(1+\frac{1}{\beta}\right)K_p\psi(\tau)\end{aligned} \tag{28}$$

$$\begin{aligned}\frac{\theta'(\tau)-\theta(\tau)}{\Delta\tau} + U\theta(\tau)\frac{(1-e^{-i\alpha\Delta X})}{\Delta X} + V\theta(\tau)\frac{(e^{i\beta\Delta Y}-1)}{\Delta Y}\\ = \left(\frac{1+R}{Pr}\right)2\theta(\tau)\frac{(cos\beta\Delta Y)-1)}{(\Delta Y)^2} + UE_c\psi(\tau)\left(1+\frac{1}{\beta}\right)\left(\frac{e^{i\beta\Delta Y}-1}{\Delta Y}\right)^2\\ + Nb\bar{C}\,\theta(\tau)\left(\frac{e^{i\beta\Delta Y}-1}{\Delta Y}\right)^2 + Nt\bar{T}\,\theta(\tau)\left(\frac{e^{i\beta\Delta Y}-1}{\Delta Y}\right)^2 + Q\theta(\tau)\end{aligned} \tag{29}$$

$$\begin{aligned}\frac{\phi'(\tau)-\phi(\tau)}{\Delta\tau} + U\phi(\tau)\frac{(1-e^{-i\alpha\Delta X})}{\Delta X} + V\phi(\tau)\frac{(e^{i\beta\Delta Y}-1)}{\Delta Y}\\ = \frac{1}{Le}\left[2\phi(\tau)\frac{cos\beta\Delta Y-1}{(\Delta Y)^2} + \frac{Nt}{Nb}\left(2\theta(\tau)\frac{cos\beta\Delta Y-1}{(\Delta Y)^2}\right)\right] - \gamma\phi(\tau)\end{aligned} \tag{30}$$

Equations (28)–(30) can be written in the following form:

$$\psi' = A_1\psi + A_2\theta + A_3\phi, \tag{31}$$

$$\theta' = B\theta + E\psi, \tag{32}$$

$$\phi' = J\phi + K\theta, \tag{33}$$

where

$$A_1 = 1 - U\frac{\Delta\tau}{\Delta X}(1 - e^{-i\alpha\Delta X}) - V\frac{\Delta\tau}{\Delta Y}(e^{i\beta\Delta Y} - 1) + \frac{\Delta\tau}{U}\left\{\frac{1}{Re}\left(\frac{b^2}{a^2}\right) + M(1-U)\right\} + \left(1 + \frac{1}{\beta}\right)\frac{2\Delta\tau}{(\Delta Y)^2}(cos\beta\Delta Y - 1) - \left(1 + \frac{1}{\beta}\right)K_p\Delta\tau,$$

$$A_2 = G_r\Delta\tau,$$

$$A_3 = G_m\Delta\tau,$$

$$B = 1 - U\frac{\Delta\tau}{\Delta X}(1 - e^{-i\alpha\Delta X}) - V\frac{\Delta\tau}{\Delta Y}(e^{i\beta\Delta Y} - 1) + \left(\frac{1+R}{Pr}\right)\frac{2\Delta\tau}{(\Delta Y)^2}(cos\beta\Delta Y - 1) + Nb\bar{C}\,\Delta\tau\left(\frac{e^{i\beta\Delta Y} - 1}{\Delta Y}\right)^2 + Nt\bar{T}\,\Delta\tau\left(\frac{e^{i\beta\Delta Y} - 1}{\Delta Y}\right)^2 + Q\Delta\tau,$$

$$E = UE_c\Delta\tau\left(1 + \frac{1}{\beta}\right)\left(\frac{e^{i\beta\Delta Y} - 1}{\Delta Y}\right)^2,$$

$$J = 1 - U\frac{\Delta\tau}{\Delta X}(1 - e^{-i\alpha\Delta X}) - V\frac{\Delta\tau}{\Delta Y}(e^{i\beta\Delta Y} - 1) + \frac{2}{Le}\frac{\Delta\tau}{(\Delta Y)^2}(cos\beta\Delta Y - 1) - \gamma\Delta\tau,$$

$$K = \frac{2}{Le}\frac{Nt}{Nb}\frac{\Delta\tau}{(\Delta Y)^2}(cos\beta\Delta Y - 1).$$

Now Equations (31)–(33) can be expressed in matrix form as:

$$\begin{bmatrix}\psi'\\ \theta'\\ \phi'\end{bmatrix} = \begin{bmatrix}A_1 & A_2 & A_3\\ E & B & 0\\ 0 & K & J\end{bmatrix}\begin{bmatrix}\psi\\ \theta\\ \phi\end{bmatrix}$$

$$\Rightarrow \eta' = T\eta$$

Where $\eta' = \begin{bmatrix}\psi'\\ \theta'\\ \phi'\end{bmatrix}$, $T = \begin{bmatrix}A_1 & A_2 & A_3\\ E & B & 0\\ 0 & K & J\end{bmatrix}$ and $\eta = \begin{bmatrix}\psi\\ \theta\\ \phi\end{bmatrix}$.

It is important to obtain the eigenvalues of the matrix T to establish the stability condition, however, this is problematic in this case as all the elements in T are different. To address this issue, an extremely short time step-size, that is, $\Delta\tau \to 0$, is suggested. As a consequence, $E \to 0$ and $K \to 0$ are obtained. The modified matrix is now:

$$T = \begin{bmatrix}A_1 & A_2 & A_3\\ 0 & B & 0\\ 0 & 0 & J\end{bmatrix}.$$

Hence the eigenvalues of the amplified matrix T are $\lambda_1 = A_1$, $\lambda_2 = B$, and $\lambda_3 = J$.

For stability, the eigenvalues cannot surpass unity in modulus. Hence the stability conditions are:

$$|A_1| \leq 1, |B| \leq 1 \quad \text{and} \quad |J| \leq 1.$$

Considering U is nonnegative and V is nonpositive everywhere and choosing $a = \Delta\tau$, $b = U\frac{\Delta\tau}{\Delta X}$, $c = |-V|\frac{\Delta\tau}{\Delta Y}$, and $d = 2\frac{\Delta\tau}{(\Delta Y)^2}$, where a, b, c, and d are real and nonnegative numbers, we have:

$$A_1 = 1 - 2\left[b + c + \left(2d + \frac{aK_p}{2}\right)\left(1 + \frac{1}{\beta}\right) - \frac{a}{2U}\left\{\frac{1}{Re}\left(\frac{b^2}{a^2}\right) + M(1-U)\right\}\right],$$

$$B = 1 - 2\left[b + c + 2d\left(\frac{1+R}{Pr} - 2Nb\bar{C} - 2dNt\bar{T}\right) - \frac{Qa}{2}\right],$$

$$J = 1 - 2\left[b + c + \frac{2d}{Le} + \frac{\gamma a}{2}\right].$$

We can say that the maximum modulus of A_1, B, and J occurs when $\alpha\Delta X = m\pi$ and $\beta\Delta Y = n\pi$, where $m = n =$ odd integer. The most negative value of A_1, B, and J that can be allowed is -1, that is, A, B, and $J \geq -1$This gives:

$$b + c + \left(2d + \frac{aK_p}{2}\right)\left(1 + \frac{1}{\beta}\right) - \frac{a}{2U}\left\{\frac{1}{Re}\left(\frac{b^2}{a^2}\right) + M(1-U)\right\} \leq 1$$

$$b + c + 2d\left(\frac{1+R}{Pr} - Nb\bar{C} - Nt\bar{T}\right) - \frac{Qa}{2} \leq 1$$

$$b + c + \frac{2d}{Le} + \frac{\gamma a}{2} \leq 1$$

That is,

$$U\frac{\Delta\tau}{\Delta X} + |V|\frac{\Delta\tau}{\Delta Y} + \left(\frac{2\Delta\tau}{(\Delta Y)^2} + \frac{K_p\Delta\tau}{2}\right)\left(1 + \frac{1}{\beta}\right) - \frac{\Delta\tau}{2U}\left[\frac{1}{Re}\left(\frac{b^2}{a^2}\right) + M(1-U)\right] \leq 1$$

$$U\frac{\Delta\tau}{\Delta X} + |V|\frac{\Delta\tau}{\Delta Y} + \frac{2\Delta\tau}{(\Delta Y)^2}\left[\frac{1+R}{Pr} - Nb\bar{C} - Nt\bar{T}\right] - \frac{Q\Delta\tau}{2} \leq 1$$

$$U\frac{\Delta\tau}{\Delta X} + |V|\frac{\Delta\tau}{\Delta Y} + \frac{1}{Le}\frac{2\Delta\tau}{(\Delta Y)^2} + \frac{\gamma\Delta\tau}{2} \leq 1$$

From the initial condition, we have $U = V = \bar{T} = \bar{C} = 0$ at $\tau = 0$ and we consider $E_c << 1$, $Q < 1.95$, and $R \geq 0.5$. Therefore, with $\Delta X = 0.8$, $\Delta Y = 0.2$, and $\Delta\tau = 0.005$, the convergence criteria for the algorithm are $Le \geq 0.25$ and $Pr \geq 0.373$.

5 | RESULTS AND DISCUSSIONS

To study the physical behavior of the problem, the influence of dimensionless parameters like Casson parameter (β), Grashof number (G_r), modified Grashof number (G_m), thermophoresis parameter (Nt), chemical reaction parameter (γ), radiation parameter (R), permeability parameter (K_p), Lewis number (Le), magnetic parameter (M), Prandtl number (Pr), and Brownian motion parameter (Nb) on velocity profile, temperature profile, and nanoparticle concentration profile are displayed in graphical representation. Here, all the graphs are obtained using numerical results via an explicit finite difference scheme in MATLAB software.

Figure 3 exhibits the variation in velocity profile for different values of M. It is observed that a rise in the magnetic parameter causes a decrease in the velocity profile. A Lorentz force is

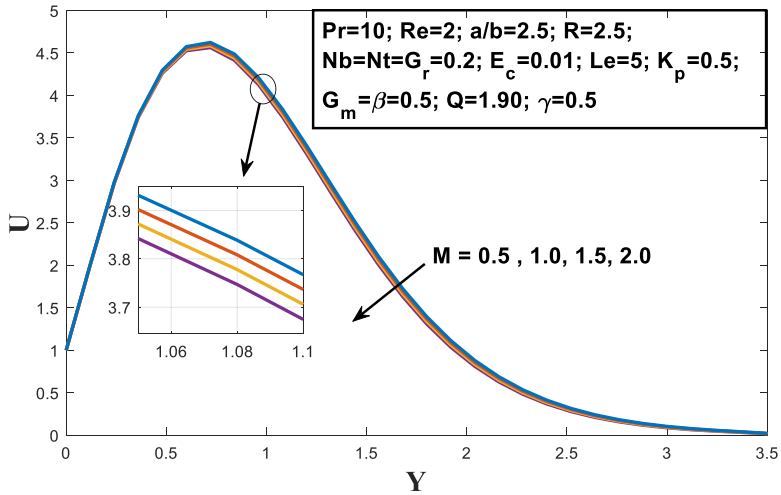

FIGURE 3 Velocity profile for different values of M

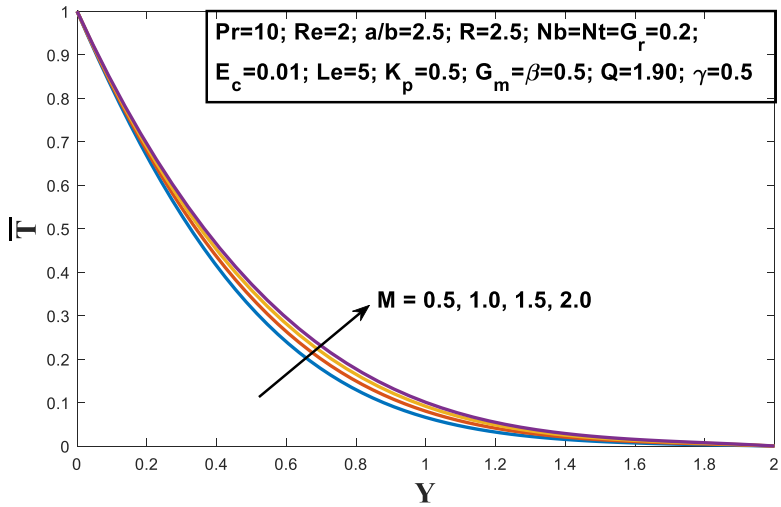

FIGURE 4 Temperature profile for different values of M

produced when a magnetic field is applied to an electrically conducting fluid. This force retards the fluid velocity in the boundary layer region as the magnetic field opposes the transport phenomena. In Figure 4, it can be observed that the temperature distribution in the boundary layer region increases with the increase in M. Due to the Lorentz force effect, the flow encounters frictional resistance, which causes the boundary layer to heat up. Consequently, the temperature rises as M increases. The effect of magnetic fields on nanofluid has many industrial applications in the cooling sector.

The temperature and nanoparticle concentration profile both rise as Nt increases, as seen in Figures 5 and 6. The explanation for this is that the rise in Nt is due to the enhancement of

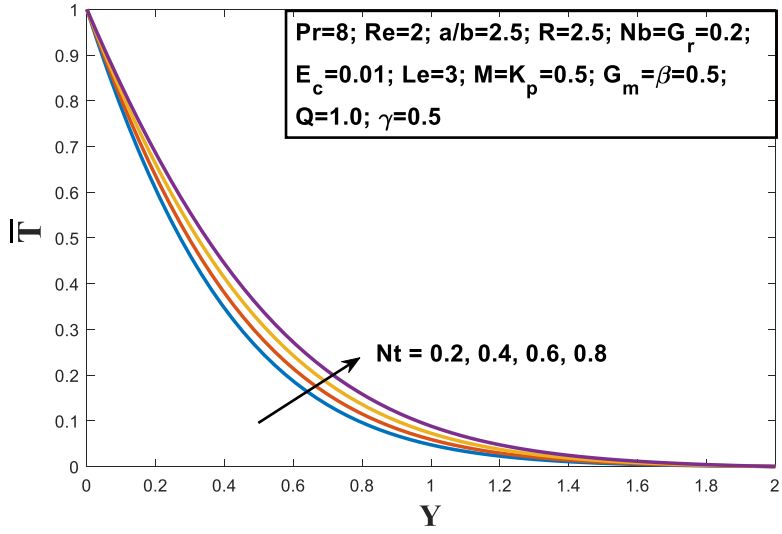

FIGURE 5 Temperature profile for different values of Nt

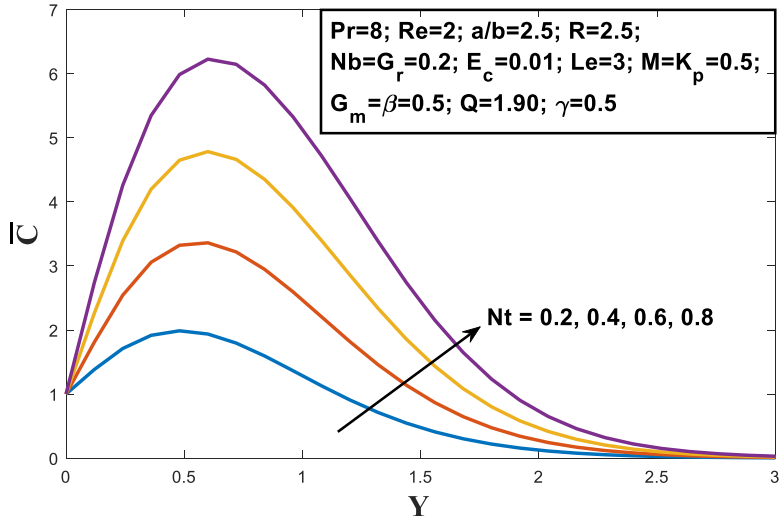

FIGURE 6 Concentration profile for different values of Nt

thermophoresis force, which tends to move nanoparticles rapidly from hot surface to cold surface away from the sheet. As a result, the nanoparticles returned from the warm surface led to an increase in the thermal curve. Again, due to this movement of the nanoparticles caused by the thermophoresis force, the concentration profile also increases.

Figure 7 reveals the influence of *Nb* on temperature. It is evident from the figure that the temperature rises as we increase the value of *Nb*. It is well known that as *Nb* increases, so does the random motion of nanoparticles, resulting in an increase in collisions with other nanoparticles. As a result, the kinetic energy is transformed into heat energy, and the temperature rises. On the other hand, Figure 8 shows the concentration profile for different values of *Nb* and it is observed that the nanoparticle volume fraction within the boundary layer

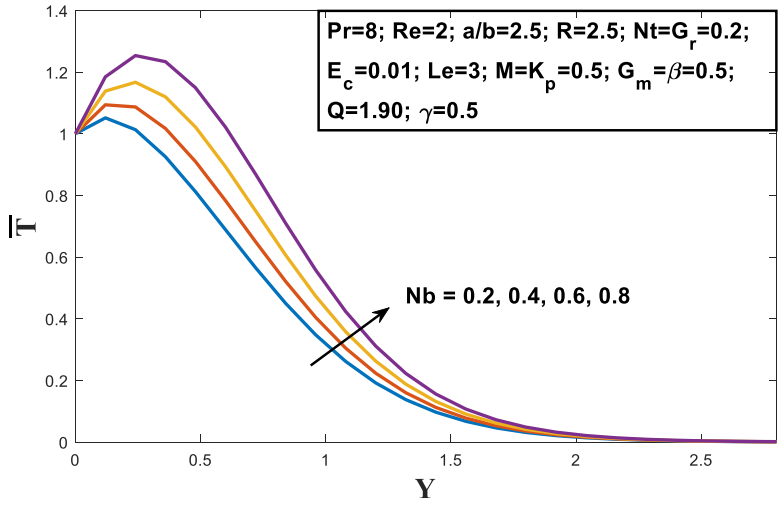

FIGURE 7 Temperature profile for different values of *Nb*

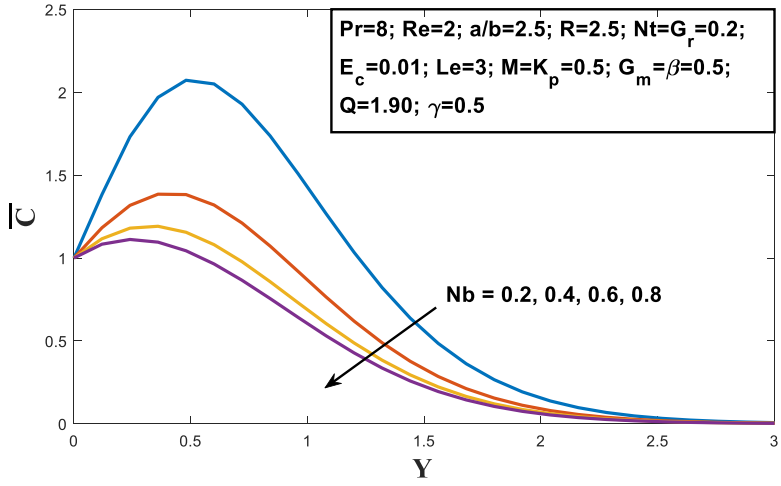

FIGURE 8 Concentration profile for different values of *Nb*

decreases with the increase in *Nb*. This is due to the tendency of the particles to get close to each other as *Nb* increases.

Figures 9 and 10 exhibits the effect of *Pr* on the dimensionless temperature and concentration profile respectively. Clearly, increasing *Pr* lowers both the temperature and the concentration of nanoparticles. *Pr* is represented by the ratio of momentum diffusivity to thermal diffusivity. Thus, with the higher value of *Pr*, the momentum diffuses more rapidly than the heat, indicating that fluids with a higher Prandtl number have low thermal conductivity and a thinner thermal layer structure. The temperature in the boundary layer region decreases with the increase in Prandtl number due to the increase in the heat transfer rate of the fluid. Whereas an increase in Prandtl number leads to a reduction in the particle distribution, which is due to the combined effect of conduction and forced convection.

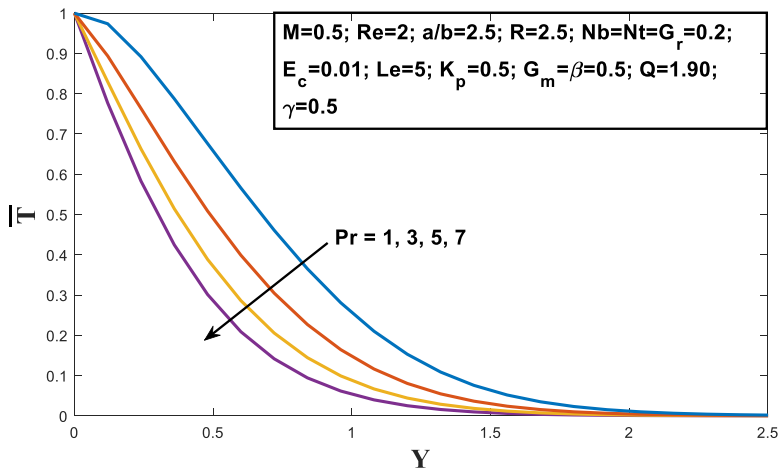

FIGURE 9 Temperature profile for different values of *Pr*

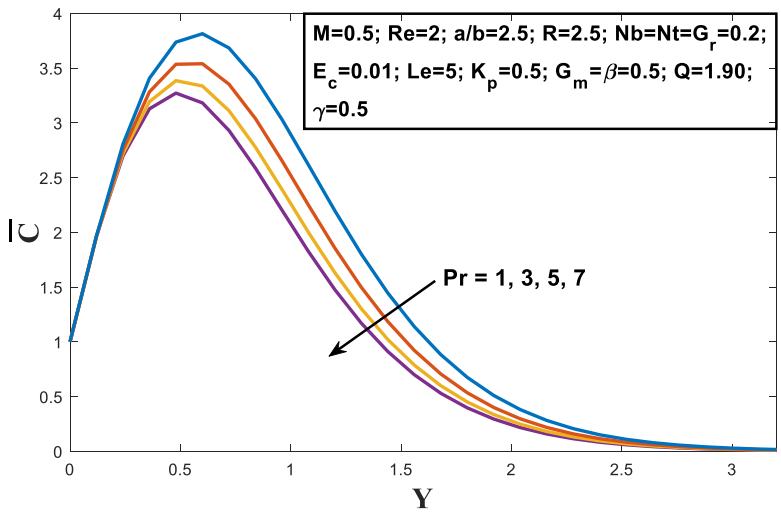

FIGURE 10 Concentration profile for different values of *Pr*

Figure 11 shows the influence of radiation parameters on the temperature profile. It can be seen that the temperature increases with the increase in radiation parameters. This is because an increase in thermal radiation causes a release of heat energy into the fluid, which is responsible for the observed phenomenon. The outcome of the chemical reaction parameter γ on the nanoparticle concentration is depicted in Figure 12. It is clear from the graph that the concentration decreases as we increase the reaction parameter. The main reason is that as the value of a chemical reaction parameter goes up, the number of solute molecules involved in the reaction also increases. This makes the concentration profile decrease. Thus, the solutal

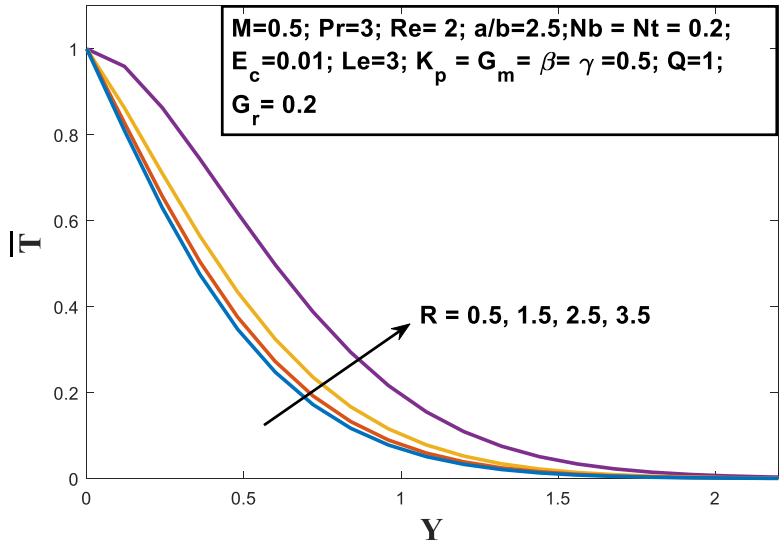

FIGURE 11 Temperature profile for different values of R

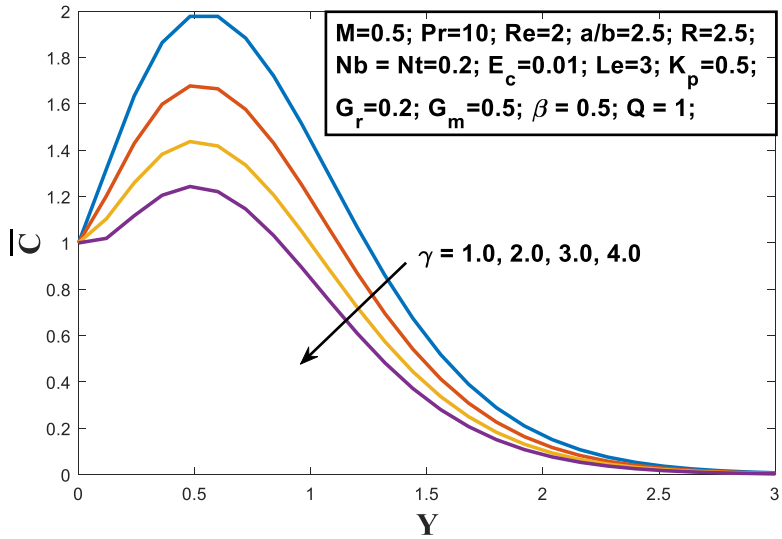

FIGURE 12 Concentration profile for different values of γ

boundary layer depletes significantly with the use of extensive chemical reactions, which leads to a rise in mass transfer phenomena.

The velocity profile is affected by the Grashof number and modified Grashof number, as seen in Figure 13. It is evident from the graph that the velocity profile rises as both parameters increase. This is due to the fact that the Grashof number is the ratio of the buoyancy force to the viscous force. Physically, the higher the value of the Grashof number, the higher the buoyancy force, which means the fluid movement is high. The same kind of explanation can be given for the effect of the modified Grashof number on the velocity profile too. Figure 14 illustrates the

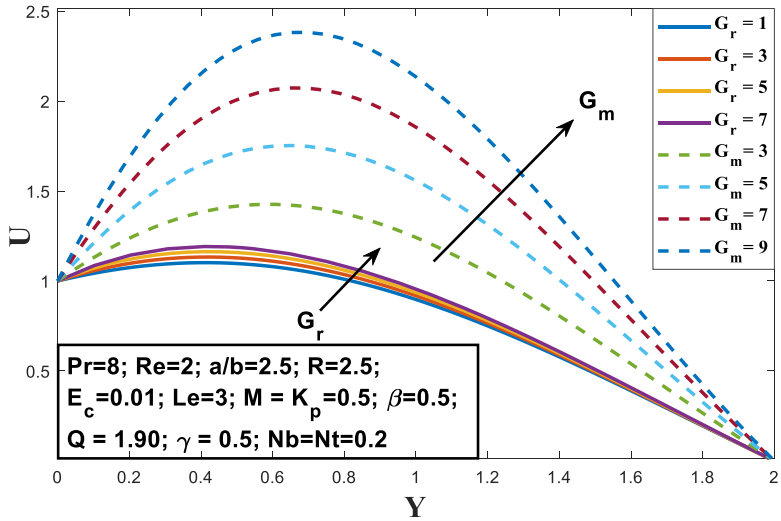

FIGURE 13 Velocity profile for different values of *Gr* and *Gm*

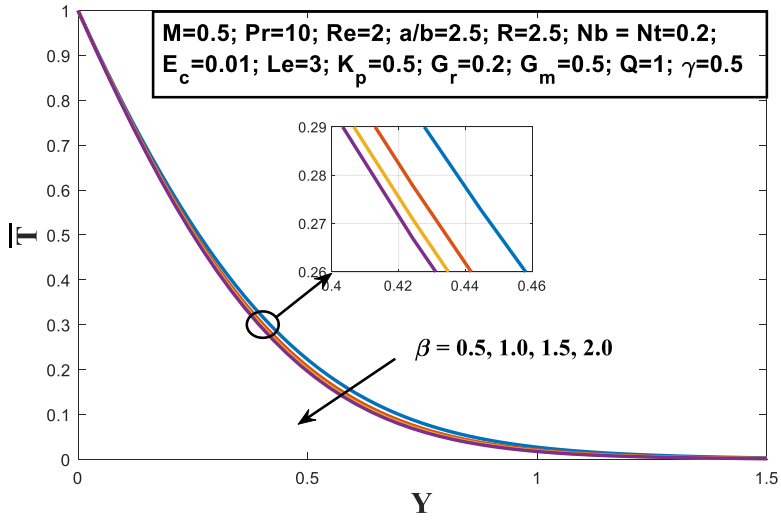

FIGURE 14 Temperature profile for different values of β

influence of the Casson parameter (β) on the temperature distribution. It can be clearly observed that the temperature decreases with the increase in the value of Casson parameter. The central reason for this phenomenon is that an increase in the Casson parameter leads to a reduction in yield stress, which in turn reduces the thickness of the thermal boundary layer. Lastly, Figure 15 reveals that the nanoparticle concentration profile decreases with the increase in Lewis number. This is because the mass transfer rate increases as the Lewis number increases. This results in an increase in the concentration gradient near the sheet. This leads to a decrease in concentration near the sheet as the Lewis number increases.

Table 1 shows the qualitative comparison of our results with that of the previous work of Bég et al.[40] and Khan et al.[19] to check the authenticity of our approach.

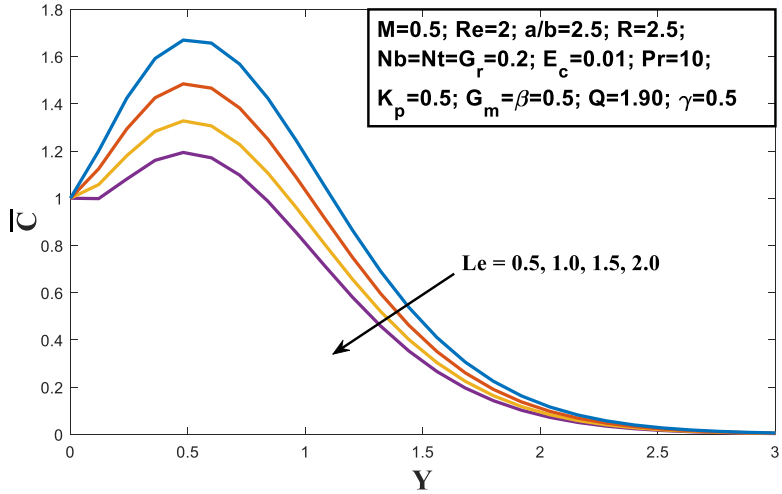

FIGURE 15 Concentration profile for different values of *Le*

TABLE 1 Comparison of the accuracy of the present results with the previous results of Khan et al. and Bég et al.

	Khan et al.[39]			Bég et al.[40]			Khan et al.[19]			Present study		
Increased parameter	U	$\bar{T}$	$\bar{C}$	U	$\bar{T}$	$\bar{C}$	U	$\bar{T}$	$\bar{C}$	U	$\bar{T}$	$\bar{C}$
M	Dec									Dec	Inc	
Nt		Inc		Inc	Inc						Inc	Inc
Nb		Inc		Inc	Inc			Inc	Dec		Inc	Dec
Pr		Dec	Dec		Dec			Dec			Dec	Dec
R				Dec				Inc	Dec		Inc	
Le			Dec						Dec			Dec
Gr	Inc			Inc						Inc		
Gm				Inc						Inc		

6 | CONCLUSIONS

A numerical investigation of two-dimensional unsteady MHD Casson nanofluid flow over a nonlinearly porous stretching sheet is presented in this article. The numerical results are obtained by implementing the finite difference scheme coded in MATLAB software. The findings are summarized below-

- The velocity profile of the nanofluid declines with the increase in the value of the magnetic parameter, whereas it increases with the increase in the value of the Grashof number and modified Grashof number.
- The thermal profile of the nanofluid escalates with the increase in magnetic parameters, Brownian motion parameter, thermophoresis parameter, and radiation parameter.
- The temperature profile of the nanofluid decelerates with the increase in the Prandtl number and Casson parameter.
- The nanoparticle volume fraction in the boundary layer region increases as the thermophoresis parameter increases, while it decreases as the Brownian motion parameter, Prandtl number, Lewis number, and chemical reaction parameter increase.
- The present study provides a model for enhanced heat transfer phenomena and hence finds its application in the cooling sector in industries, postaccidental heat removal in nuclear reactors, and heat exchangers. Besides these, some other important scientific applications of this study may be relevant to manufacturing industries, solar collectors, and so on.

NOMENCLATURE

t	time (s)
x, y	Cartesian coordinates tangential to the surface and normal to it, respectively (m)
X, Y	dimensionless Cartesian coordinates along the surface and normal to it, respectively
u, v	velocity components along x-axis and y-axis respectively (ms^{-1})
U, V	dimensionless velocity components along x-axis and y-axis, respectively
T	temperature (K)
C	nanoparticle concentration ($mol\,L^{-1}$)
$\overline{T}$	dimensionless temperature
$\overline{C}$	dimensionless nanoparticle concentration
B	magnetic field strength (T)
g	acceleration due to gravity (ms^{-2})
k_o	porous term (m^2)
C_p	specific heat at constant pressure ($J\,kg^{-1}\,K^{-1}$)
D_B, D_T	co-efficient of Brownian and thermophoretic diffusion respectively ($m^2\,s^{-1}$)
q_r	radiative heat flux
Q_o	heat sink/source coefficient
K_1	reaction coefficient
M	magnetic parameter
Re	Reynolds number
a/b	velocity parameter
G_r	Grashof number
G_m	modified Grashof number
K_p	permeability parameter
E_c	Eckert number

Pr	Prandtl number
R	radiation parameter
Nb	Brownian motion parameter
Nt	thermophoresis parameter
Q	heat source/sink parameter
Le	Lewis number

GREEK SYMBOLS

τ	dimensional time variable
υ	kinematic viscosity ($m^2\ s^{-1}$)
β	Casson parameter
σ_e	electrically conductivity ($S\ m^{-1}$)
ρ	density ($kg\ m^{-3}$)
β_t	coefficient of thermal expansion
β_c	coefficient of concentration expansion
α	thermal diffusivity ($m^2\ s^{-1}$)
τ^*	ratio between effective heat capacity of nanoparticles to effective heat capacity of base fluid
γ	chemical reaction parameter

SUFFIX

w	at wall
∞	at free stream region

DATA AVAILABILITY STATEMENT

Data sharing is not applicable to this article as no datasets were generated or analysed during the current study.

ORCID

Shiva Rao https://orcid.org/0000-0003-2055-4441
Paramananda Deka https://orcid.org/0000-0001-9485-9294

REFERENCES

1. Choi SUS. Enhancing thermal conductivity of fluids with nanoparticles. *ASME Int Mech Eng Congress Exposit*. 1995;66:99-105.
2. Lee S, Choi SUS, Li S, Eastman JA. Measuring thermal conductivity of fluids containing oxide nanoparticles. *ASME J Heat Transfer*. 1999;121(2):280-289.
3. Otanicar TP, Phelan PE, Prasher RS, Rosengarten G, Taylor RA. Nanofluid-based direct absorption solar collector. *J Renew Sustain Energy*. 2010;2(3):033102.
4. Eastman JA, Choi SUS, Li S, Yu W, Thompson LJ. Anomalously increased effective thermal conductivities of ethylene glycol-based nanofluids containing copper nano-particles. *Appl Phys Lett*. 2001;78(6):718-720.
5. Buongiorno J. Convective transport in nanofluids. *J Heat Transfer*. 2006;128(3):240-250.
6. Kuznetsov AV, Nield DA. Natural convective boundary-layer flow of a nanofluid past a vertical plate. *Int J Therm Sci*. 2010;49(2):243-247.
7. Khan WA, Pop I. Boundary-layer flow of a nanofluid past a stretching sheet. *Int J Heat Mass Transfer*. 2010;53(11):2477-2483.
8. Makinde OD, Aziz A. Boundary layer flow of a nanofluid past a stretching sheet with a convective boundary condition. *Int J Therm Sci*. 2011;50(7):1326-1332.

9. Rana P, Bhargava R. Flow and heat transfer of a nanofluid over a nonlinearly stretching sheet: A numerical study. *Commun Nonlin Sci Num Simul*. 2012;17(1):212-226.
10. Khan ZH, Makinde OD, Hamid M, Rizwan UH, Khan WA. Hydromagnetic flow of ferrofluid in an enclosed partially heated trapezoidal cavity filled with a porous medium. *J Magn Magn Mater*. 2020;499:166241.
11. Hosseinzadeh K, Mardani MR, Salehi S, Paikar M, Ganji DD. Investigation of micropolar hybrid nanofluid (iron Oxide–Molybdenum disulfide) flow across a sinusoidal cylinder in presence of magnetic field. *Int J Appl Comput Math*. 2021;7:210.
12. Zangooee MR, Hosseinzadeh K, Ganji DD. Investigation of three-dimensional hybrid nanofluid flow affected by nonuniform MHD over exponential stretching/shrinking plate. *Nonlin Eng*. 2022;11(1):143-155.
13. Hosseinzadeh S, Hosseinzadeh K, Hasibi A, Ganji DD. Hydrothermal analysis on non-newtonian nanofluid flow of blood through porous vessels. *Proc Institut Mech Eng J Process Mech Eng*. 2022;236(4):1604-1615.
14. Akbar N, Khan Z, Nadeem S, Khan W. Double-diffusive natural convective boundary-layer flow of a nanofluid over a stretching sheet with magnetic field. *Int J Num Methods Heat Fluid Flow*. 2016;26(1):108-121.
15. Reddy MG, Rani MVVNLS, Praveen MM, Kumar KG. Comparative study of different non-newtonian fluid over an elaborated sheet in the view of dual stratified flow and ohmic heat. *Chem Phys Lett*. 2021;784:139096.
16. Rostami HT, Najafabadi MF, Hosseinzadeh K, Ganji DD. Investigation of mixture-based dusty hybrid nanofluid flow in porous media affected by magnetic field using RBF method. *Int J Ambient Energy*. 2022:1-11. doi:10.1080/01430750.2021.2023041
17. Ahmad S, Khan ZH, Zeb S, Hamid M. Thermal and entropy generation analysis of magnetohydrodynamic tangent hyperbolic slip flow towards a stretching sheet. *Proc Institut Mech Eng J Process Mech Eng*. 2022;236(2):357-367.
18. England WG, Emery AF. Thermal radiation effects on the laminar free convection boundary layer of an absorbing gas. *ASME J Heat Transfer*. 1969;91(1):37-44.
19. Khan MS, Alam MM, Tzirtzilakis EE, Ferdows M, Karim I. Finite difference simulation of MHD radiative flow of a nanofluid past a stretching sheet with stability analysis. *Int J Adv Thermofluid Res*. 2016;2:31-46.
20. Kumar MA, Reddy YD, Rao VS, Goud BS. Thermal radiation impact on MHD heat transfer natural convective nano fluid flow over an impulsively started vertical plate. *Case Stud Thermal Eng*. 2021;24:100826.
21. Ali A, Kanwal T, Awais M, Shah Z, Kumam P, Thounthong P. Impact of thermal radiation and non-uniform heat flux on MHD hybrid nanofluid along a stretching cylinder. *Sci Rep*. 2021;11(1):20262.
22. Ahmed MM, Reddy MG, Abbas W. Modeling of MHD fluid flow over an unsteady stretching sheet with thermal radiation, variable fluid properties and heat flux. *Math Comput Simul*. 2021;185(C):583-593.
23. Lv YP, Shaheen N, Ramzan M, Mursaleen M, Nisar KS, Malik MY. Chemical reaction and thermal radiation impact on a nanofluid flow in a rotating channel with Hall current. *Sci Rep*. 2021;11(1):19747.
24. Devi SVVR, Reddy MG. Parametric analysis of MHD flow of nanofluid in stretching sheet under chemical sensitivity and thermal radiation. *Heat Transfer*. 2022;51:948-975.
25. Ibrahim SM, Lorenzini G, Kumar PV, Raju CSK. Influence of chemical reaction and heat source on dissipative MHD mixed convection flow of a Casson nanofluid over a nonlinear permeable stretching sheet. *Int J Heat Mass Transfer*. 2017;111:346-355.
26. Reddy MG, Polarapu P, Gorla RSR. Influence of double stratification on MHD three dimensional casson nanofluid flow over a stretching sheet: a numerical study. *J Nanofluids*. 2017;6(1):71-79(9).
27. Shashikumar NS, Archana M, Prasannakumara BC, Gireesha BJ, Makinde OD. Effects of nonlinear thermal radiation and second order slip on Casson nanofluid flow between parallel plates. *Defect Diffusion Forum*. 2017;377:84-94.
28. Rafique K, Anwar MI, Misiran M, et al. Numerical solution of Casson nanofluid flow over a non-linear inclined surface with soret and Dufour effects by Keller-Box method. *Front Phys*. 2019;7:00139.
29. Lund LA, Omar Z, Khan I, Sherif ESM, Abdo HS. Stability analysis of the magnetized Casson nanofluid propagating through an exponentially shrinking/stretching plate: dual solutions. *Symmetry*. 2020;12(7):1162.

30. Abdal S, Hussain S, Siddique I, Ahmadian A, Ferrara M. On solution existence of MHD Casson nanofluid transportation across an ex-tending cylinder through porous media and evaluation of priori bounds. *Sci Rep*. 2021;11(1):7799.
31. Reza-E-Rabbi Sk, Arifuzzaman SM, Sarkar T, Khan MS, Ahmmed S. Explicit finite difference analysis of an unsteady MHD flow of a chemically reacting Casson fluid past a stretching sheet with Brownian motion and thermophoresis effects. *J King Saud Univ–Sci*. 2020;32(1):690-701.
32. Mukhopadhyay S, Vajravelua K, Van Gorder RA. Casson fluid flow and heat transfer at an exponentially stretching permeable surface. *J Appl Mech*. 2013;80:054502.
33. Oyelakin IS, Mondal S, Sibanda P. Unsteady Casson nanofluid flow over a stretching sheet with thermal radiation, convective and slip boundary conditions. *Alex Eng J*. 2016;55:1025-1035.
34. Pai SI. Viscous flow theory. *Laminar Flow*. Vol 1. D. VanNostrand Co; 1956.
35. Schichting H. *Boundary Layer Theory*. McGraw-Hill; 1964:6.
36. Brewster MQ. *Thermal Radiative Transfer Properties*. John Wiley and Sons; 1972.
37. Sparrow EM, Cess RD. *Radiation Heat Transfer*. Hemisphere; 1978.
38. Raptis A. Radiation and free convection flow through a porous medium. *Int Commun Heat Mass Transf*. 1998;25:289-295.
39. Khan MS, Wahiduzzaman M, Uddin MS, Sazad MAK. Finite difference solution of MHD free convection heat and mass transfer flow of a nanofluid along a stretching sheet with heat generation effects. *Indian J Theor Phys*. 2012;60:285-306.
40. Bég OA, Khan MS, Karim I, Alam MM, Ferdows M. Explicit numerical study of unsteady hydromagnetic mixed convective nanofluid flow from an exponentially stretching sheet in porous media. *Appl Nanosci*. 2014;4:943-957.

How to cite this article: Rao S, Deka P. A numerical solution using EFDM for unsteady MHD radiative Casson nanofluid flow over a porous stretching sheet with stability analysis. *Heat Transfer*. 2022;51:8020-8042. doi:10.1002/htj.22679